Mixing in coaxial jets

By E. VILLERMAUX AND H. REHAB

IRPHE, Universite de Provence, Centre de Saint Jérôme Service 252,
13397 Marseille Cedex 20, France

The stirring and mixing properties of one-phase coaxial jets, with large outer (annular) to inner velocity ratio $r_u = u_2/u_1$ are investigated. Mixing is contemplated according to its geometrical, statistical and spectral facets with particular attention paid to determining the relevant timescales of the evolution of, for example, the interface area generation between the streams, the emergence of its scale-dependent (fractal) properties and of the mixture composition after the mixing transition. The two key quantities are the vorticity thickness of the outer, fast stream velocity profile which determines the primary shear instability wavelength and the initial size of the lamellar structures peeled-off from the slow jet, and the elongation rate $\gamma = (u_2 - u_1)/e$ constructed with the velocity difference between the streams and the gap thickness e of the annular jet. The kinetics of evolution of the interface corrugations, and the rate at which the mixture evolves from the initial segregation towards uniformity is prescribed by γ^{-1}. The mixing time t_s, that is the time needed to bring the initial scalar lamellae down to a transverse size where molecular diffusion becomes effective, and the corresponding dissipation scale $s(t_s)$ are

$$t_s \sim \frac{Sc^{1/5}}{\gamma}, \quad s(t_s) \sim e Re^{-1/2} Sc^{-2/5},$$

where Re and Sc denote the gap Reynolds number and the Schmidt number, respectively. The persistence of the large-scale straining motion is also apparent from the spectra of the scalar fluctuations which exhibit a k^{-1} shape on the inertial range of scales.

1. Introduction

When two fluid streams liable to react chemically merge, the extent and topology of the reaction zone coincide, provided the chemical reaction has very fast kinetics, with the region of diffusive interpenetration between the streams. This is the so-called high Damköhler number limit (see e.g. Williams 1985; Dimotakis 1991). Most exothermic combustion reactions (some simple reactions in liquids such as acido-basic neutralizations, for example), in practice, occur within this limit.

In that case, the contacting geometry and the stirring conditions just after contact play a crucial role on the overall consumption rate since they set the extent of the diffusion front between the phases.

The use of coaxial jets is widespread in the context of 'airblast atomization', that is to say high-speed gas assisted spray formation (Lefebvre 1989). The coaxial jets geometry, operating with a large outer (annular) to inner (central) momentum ratio is used for its ability to destabilize, fragment and mix the central stream in the outer, rapid stream.

Aside from the atomization context and in spite of their potential practical use-fulness, few studies have discussed the quantitative mixing properties in the field near from the injector outlet. Beér & Lee (1965) have measured the residence time distribution (RTD) of tracer particles injected into the central jet, and have linked the shape of the RTD with the operating parameters. The complex interaction of the instabilities resulting from the development of the two nearby shear layers (one between the inner jet and the outer jet, and the other between the outer jet and the surrounding medium) have been documented in one-phase coaxial jets by Dahm, Clifford & Tryggvanson (1992).

Rehab, Villermaux & Hopfinger (1997) have studied the flow regimes in the near field as the velocity ratio between the streams is varied. These authors have, in particular, shown how the velocity ratio determines the inner jet potential core length, and the condition for a recirculation, wakelike transition, which occurs when the velocity ratio is increased above a critical value.

At the root of the interpenetration between the phases is a strong shear. Since the disturbances at the interface between the streams are convected by the mean flow, this geometry offers the opportunity of following in space the precise sequence of events which contribute to the interpenetration between the phases subsequent to the development of the shear instability, up to the onset of molecular mixing and diffusive uniformity of the mixture.

Plane shear layer experiments have emphasized the role of the persistent large-scale motions on the interpenetration between the phases, and have determined how the spreading rate of the resulting 'mixing layer' depends on their velocity ratio (Brown & Roshko 1974). In this configuration, the existence of a 'mixing transition' has been shown (Breidenthal 1981), and the evolution of the medium composition after the transition has been documented (Koochesfahani & Dimotakis 1986), as well as its sensitivity to the initial contacting conditions (Huang & Ho 1990; Karasso & Mungal 1996; Slessor, Bond & Dimotakis 1998).

The internal structure of the concentration field in a mixture can be investigated through the spatial scaling of the concentration increment distributions with the separation distance. In particular, the second-order moment of the distributions, equivalently the power spectrum of the concentration fluctuations, has led to predictions based on cascade arguments (Oboukhov 1949; Corrsin 1951; Batchelor 1959) that are currently critically checked (see e.g. Sreenivasan 1996 for a review). The relation of the spectral signature of a mixture with its mixing state is still unclear.

The multiscale geometry of a passive interface immersed in a disordered flow has long been recognized (Welander 1955) and has stimulated, guided by the concept of fractal objects, a large amount of work (see e.g. Sreenivasan 1991 for a review; Catrakis & Dimotakis 1996 and references therein). Mixing is, in essence, a process dependent on time. The link between the transient shape of a scalar blob being mixed in a flow, the birth and death of its multiscale structure and the composition histogram of the scalar field has been recently established (Villermaux & Innocenti 1999).

In the present coaxial jet flow, the geometrical, structural and statistical facets of the mixture, evolving from a complete segregation at the injector outlets, to a state where the concentration levels are continuously distributed farther downstream, are examined concomitantly and put in relation to each other. We first describe the nature and mechanism of the basic shear instability between the outer and the inner stream. From there, an 'entrainment velocity' is derived which allows us to discuss the dependencies of the dilution lengths of a scalar injected in the central jet on
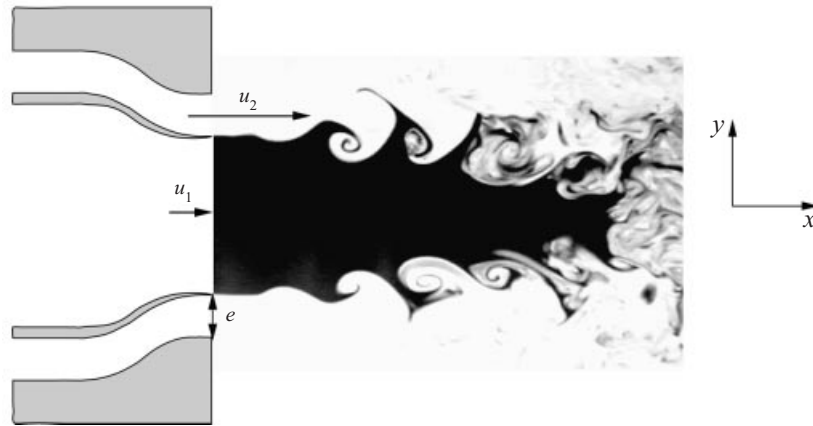
FIGURE 1. Sketch of the injector outlets and development of the flow. Inner and outer jets have diameters $D_1 = 2$ cm and $D_2 = 2.7$ cm, and velocities u_1 and u_2, respectively.

the velocity ratio, and on the concentration level chosen to define this length (§ 3). Then, we depict in detail the process of interface area generation between the streams (§ 4.1) and the emergence of scale-dependent corrugations of the interface (§ 4.2). The shear-induced thinning of the initial disturbances in the approach of the onset of molecular mixing is analysed quantitatively (§ 4.3). The evolution of the medium composition after the onset of molecular mixing is presented (§ 4.4) as well as the spectral properties of the mixture (§ 5). Finally, we discuss the possible relevance of this case study for the problem of turbulent mixing.

2. Set-up and procedures

2.1. *Flow configuration*

Two coaxial injectors are supplied with water by a constant-head reservoir and discharge into a large tank of water at rest. The flowrates are controlled by precision valves and electromagnetic flowmeters. Premixing chambers far upstream on the feeding lines allow both streams to be seeded with a fluorescent dye. The diameters of the inner and the outer jet nozzles are $D_1 = 2$ cm and $D_2 = 2.7$ cm with a contraction ratio of 2 and 4, respectively (figure 1). The mean velocities at the nozzles exit are in the ranges $0.1 < u_1 < 1 \, \mathrm{m \, s^{-1}}$ and $0.3 < u_2 < 4 \, \mathrm{m \, s^{-1}}$.

We are interested in the regime in which the ratio of the maximal velocities of the outer to the inner jet $r_u = u_2/u_1$ is larger than unity. The overall Reynolds number defined from the net momentum input is, for $r_u \gg 1$, $Re_M = (u_2 D_2/v)[1 - (D_1/D_2)^2]^{1/2}$ and is of the order of 5.4×10^3 to 7×10^4. The Reynolds number constructed on the gap thickness $e = (D_2 - D_1)/2$ and the annular momentum dominating stream velocity u_2, $Re = u_2 e/v$ ranges from 10^3 to 1.4×10^4. Residual turbulence levels represent less than 5% of the mean velocities in both streams.

The vorticity thickness δ of the rapid stream at the lip of the injector exit is such that $\delta/e = 9.5 Re^{-1/2}$, giving a Reynolds number $Re_\delta = u_2 \delta/v$ about 800 at $u_2 = 2 \, \mathrm{m \, s^{-1}}$. The thicknesses of the boundary layers on each side of the gap actually represent a small fraction of the gap width, of the order of $1/10$, in the range of Reynolds number investigated (see also Rehab *et al.* 1997).

2.2. *Measurement methods*

The images of the scalar field of the dye, diluted in one or the other stream, were obtained by a standard laser induced fluorescence technique, using disodium fluorescein as a laser fluorescent dye, whose Schmidt number, the ratio of the kinematic viscosity v to the molecular diffusivity of the dye D is about $Sc = v/D \approx 2000$. A thin laser sheet is produced by spanning a 5.4 W argon-ion laser beam, collimated by a long focal-length lens ($f = 2$ m) with a mirror oscillating at 4 kHz. This provides a uniformly illuminated region in the visualization window. The images are captured by a SONY D7CE video camera with a Paillard 75 mm f/2.8 lens at a rate of 25 images per second and an exposure time of 1/1000 s. They were either directly digitized by a NEOTECH 8 bits A/D converter and written to the computer disk, or stored on an S-VHS magnetoscope, and further digitized and processed. The images are initially digitized on 768×512 pixels and were shrunk to 384×256 pixels before processing. The calibration of the background-substracted images is linear up to the injection concentration $C_0 = 5 \times 10^{-7}$ mol l^{-1}, corresponding to a grey level of about 200. This diluted injection concentration level results in a negligible laser attenuation across the visualization window. The r.m.s. noise of the images never exceeds 1%.

The pixel size on a final image corresponds to a real dimension of 150 μm and since the thickness of the laser sheet is of the order of 300 μm, each pixel receives a fluorescence signal integrated on a $150 \times 150 \times 300$ μm^3 volume.

The dissipation lengthscale, that we denote $s(t_s)$, relevant to that configuration will be shown (see §4.2) to be $s(t_s)/e = 16Re^{-1/2}Sc^{-2/5}$ and is of the order of the resolution of the final images for the smallest gap Reynolds numbers investigated. Most of the results reported here are based on slightly under-resolved images for which $s(t_s)$ is approximately half a pixel.

Long temporal traces of the advected scalar field were obtained by a series of concentration measurements, using a fibre optic concentration probe. The probe consists of two optical fibres, with a core 200 μm thick, and whose extremities are joined and placed at right angles to each other. The emitting fibre is coupled to an argon-ion laser and the receiving fibre conveys the fluorescence light emitted in the measurement volume to a photodiode. The measurement volume is the intersection of the optical paths of the two fibres, and provides a resolution of the order of the fibre diameter (§5). The signal delivered by the photodiode was checked to be proportional to the amount of dye present in the measurement volume.

Velocity measurements were performed by a standard hot-film anemometry technique using a TSI probe with an active length of 250 μm.

3. Shear instability and entrainment

3.1. *Primary instability*

This study concentrates on the limit where the central jet carries significantly less momentum as compared to the outer jet. The inner jet is entrained and mixed by the motions originating from the destabilization of the outer jet. Since the density of both jets and of the medium at rest in which they issue is uniform, we are therefore concerned with a velocity ratio $r_u = u_2/u_1$ larger than unity. The other limit is the case of the simple jet.

Actually, the near field of coaxial jets is characterized by the existence of two shear layers, the outer one between the core of the annular jet and the surrounding medium at rest, absorbing a velocity difference $\Delta u = u_2 - 0 = u_2$, and the inner

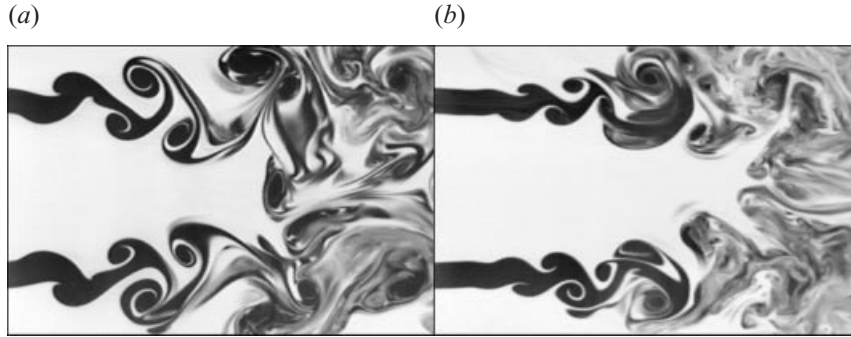(*a*)   (*b*)

FIGURE 2. Instantaneous planar cuts containing the jet axes of the near field of coaxial jets. The annular jet is seeded with a fluorescent dye and the velocity ratio is $r_u = u_2/u_1 = 4$ for both pictures. (*a*) $Re = u_2 e/v = 700$. (*b*) $Re = 1400$.

one, between the annular jet and the central jet, absorbing a velocity difference $\Delta u = u_2 - u_1 = u_2(1 - 1/r_u)$. When the vorticity thickness $\delta \sim (D_2 - D_1)Re^{-1/2}$ of the boundary layers of the velocity profile at the injector exit is not negligibly small compared to the gap width e, the inner and outer shear layers interact, giving rise to complex vorticity dynamics, resulting essentially in a sinuous instability mode, with possible phase jumps due to the difference of group velocities between the layers (see e.g. Squire 1953; Dahm *et al.* 1992).

However, as shown in figure 2, for a given gap width e, the vorticity thicknesses δ of the annular velocity profile become smaller as u_2 is increased, and the instabilities of each shear layer develop progressively, independently of each other. Their features (wavelength, group velocity) are all close to each other because the velocity ratio r_u is large at fixed u_1. We will therefore, for the sake of simplicity, assume that a single layer develops its instability as in an infinite medium. We will also consider the instability problem in the plane approximation, the thickness of the sheet δ being small compared to its spanwise radius of curvature $\frac{1}{2}D_1$ (i.e. $\delta/\frac{1}{2}D_1 \sim ((D_2/D_1) - 1)Re^{-1/2}$). Our aim is to derive the instability wavelength and its associated growth rate to estimate an entrainment velocity of the slow phase by the rapid one.

A free shear layer presenting an inflectional velocity profile is unstable in the sense initially depicted by Helmholtz & Kelvin for the case of a sharp discontinuity of velocity. This result was soon generalized by Rayleigh (1880) to the case of a finite non-zero-layer thickness with a uniform shear adapting the low-speed to the high-speed stream. Expanding the disturbances to the basic flow in Fourier modes proportional to $\exp(ikx - i\omega t))$ and letting $\kappa = k\delta$, $\Omega = \omega/k(u_2 - u_1)$ with δ the thickness the profile, the dispersion relation is found in the form

$$e^{-2\kappa} = [1 - \kappa(2\Omega + 1)][1 + \kappa(2\Omega - 1)]. \tag{1}$$

The layer is unstable for all wavenumbers such that $k\delta < 1.28$, and the maximal growth rate $r = \max[\mathrm{Re}\,\{-i\omega\}]$, corresponding to $k_m\delta \approx 0.8$, is such that $r \approx 0.2$ $(u_2 - u_1)/\delta$. The numerical factors are weakly sensitive to the detailed shape of the velocity profile (see e.g. Esch 1957) so that the piecewise linear profile is actually a generic caricature. The generalization of the dispersion equation (1) to the case where the two streams have different densities, with surface tension at the interface, has been made in Villermaux 1998*a* in connection with atomization studies. The growth rate r and most amplified wavenumber k_m are insensitive to viscosity as soon as the Reynolds number constructed on the velocity jump and the thickness of the layer
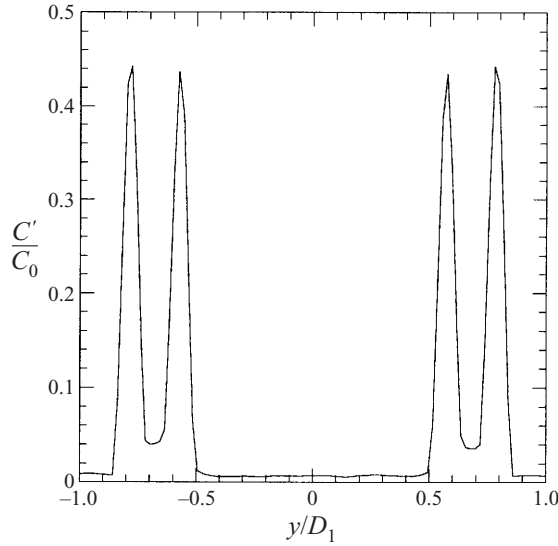
FIGURE 3. Radial profile of the r.m.s. fluctuations of concentration at $x/e = 3$, $Re = 1400$.

$(u_2 - u_1)\delta/v$ is larger than about 150 (Betchov & Szewczyk 1963; Villermaux 1998b), as it is always the case in these experiments.

The development of the shear instability between the streams is reflected by the downstream evolution of the mean concentration thickness δ_c defined by

$$\delta_c = C_0 / \left(\frac{\mathrm{d}\bar{C}}{\mathrm{d}y}\right)_{\max}, \qquad (2)$$

where $(\mathrm{d}\bar{C}/\mathrm{d}y)_{\max}$ denotes the maximum value of the gradient of the mean concentration profile in the y-direction across the shear layer (figure 3). At short times, or at short distances from the injector outlet, when molecular diffusion has not yet set in, that is as long as the instantaneous scalar field remains binary, composed of sheets bearing the injection concentration, the thickness δ_c is a measure of the mean transverse width of the layer, itself reflecting the instability amplitude to some proportionality factor.

As emphasized in the next section, the scalar field remains essentially fully segregated up to the first roll-up of the shear layer and farther. The r.m.s. fluctuation concentration at a given point in the flow $C' = \sqrt{\langle((C(t) - \bar{C})^2)\rangle}$ normalized to the injection concentration C_0 is for a binary concentration field given by $C'/C_0 = \sqrt{(\bar{C}/C_0)(1 - \bar{C}/C_0)}$, and peaks at 1/2 for $\bar{C}/C_0 = 1/2$. Figure 3 shows how the presence of the inner and outer shear layers results in two symmetrical maxima for C'/C_0 reaching about 0.45, slightly below the expected maximum and slightly above the value measured in the early development of a plane mixing layer by Bernal & Roshko (1986) who found $C'/C_0 \approx 0.35$.

As shown in figure 4, δ_c first increases exponentially in the x-direction, before reaching a plateau when the initial concentration difference C_0 is absorbed on a distance of the order of the gap width e, that is when $(C_0/e)/(\mathrm{d}\bar{C}/\mathrm{d}y)_{\max} = \delta_c/e \approx 1$.

The distance x_c at which the condition $\delta_c/e = 1$ is reached corresponds qualitatively to the formation of the first roll-up and is related to the 'wave breaking length' described by Becker & Massaro (1968) in a single round jet. It is found to decrease
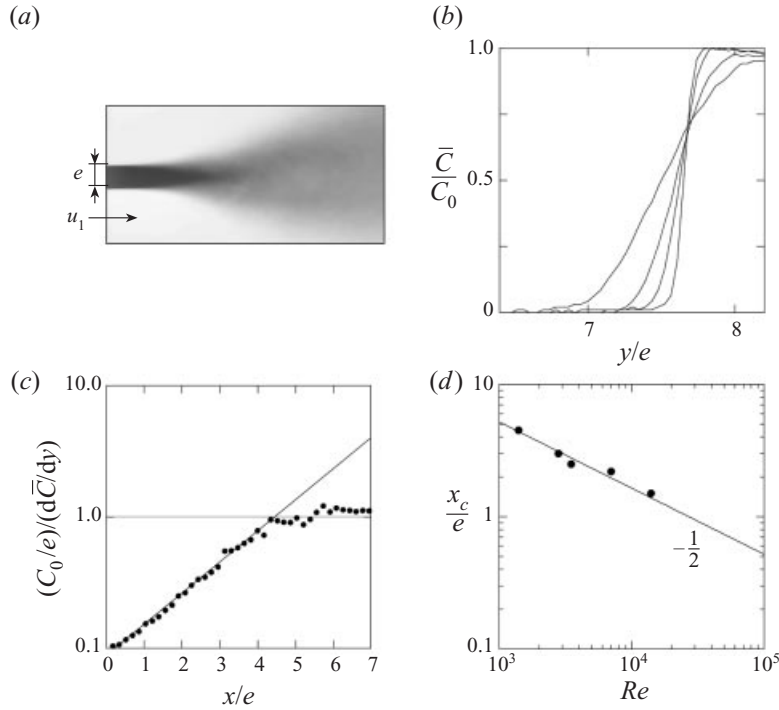
(a)

(b)

(c)

(d)

FIGURE 4. (a) Close-up of the average concentration field of the inner (top) and outer (bottom) layers on a planar cut containing the jets axis; $u_2 = 0.4\,\mathrm{m\,s^{-1}}$, $r_u = 4$, $Re = 1400$. (b) Downstream evolution of the average concentration profiles across the inner layer for $x/e = 1, 2, 3$ and 4. (c) Normalized concentration thickness δ_c/e versus downstream distance x/e. (d) Critical distance for which $\delta_c/e = 1$ as a function of the gap Reynolds number.

proportionally to the initial vorticity thickness of the fast stream velocity profile when the gap Reynolds number Re is increased. The distance x_c is also proportional to the wavelength λ selected by the shear instability giving (figure 4d),

$$\frac{x_c}{e} = 164 Re^{-1/2}, \quad \frac{\lambda}{e} = 75 Re^{-1/2}. \tag{3}$$

The wavelength in equation (3) is quantitatively consistent with the mode selected in the instability of the Rayleigh profile, i.e. $k_m\delta \approx 0.8$ (equation (1)). The spatial growth rate of the concentration thickness δ_c is well estimated in order of magnitude from a simple transformation relating time to space via the mean convection velocity $\bar{u} = u_2(1 + 1/r_u)/2$ (i.e. $t = x/\bar{u}$). With $r = 0.2u_2(1 - 1/r_u)/\delta$, $\delta/e = 9.5 Re^{-1/2}$ and $Re = 1400$, it is found that $rt = 0.94x/e$ when the numerical prefactor measured on figure 4(c) is 0.54. The quantitative difference can be attributed to at least two factors: the use of the Gaster transformation ($x = \bar{u}t$) to infer the spatial growth rate from the temporal growth rate which is known, depending on the initial shape of the profile, to induce significant differences (Monkewitz & Huerre 1982; Freymuth 1966), and the fact that we have neglected the radius of curvature of the layer. The recourse to equation (1) is only meant to discuss the origin of the instability and selected wavelength dependence on the velocity profile shape.
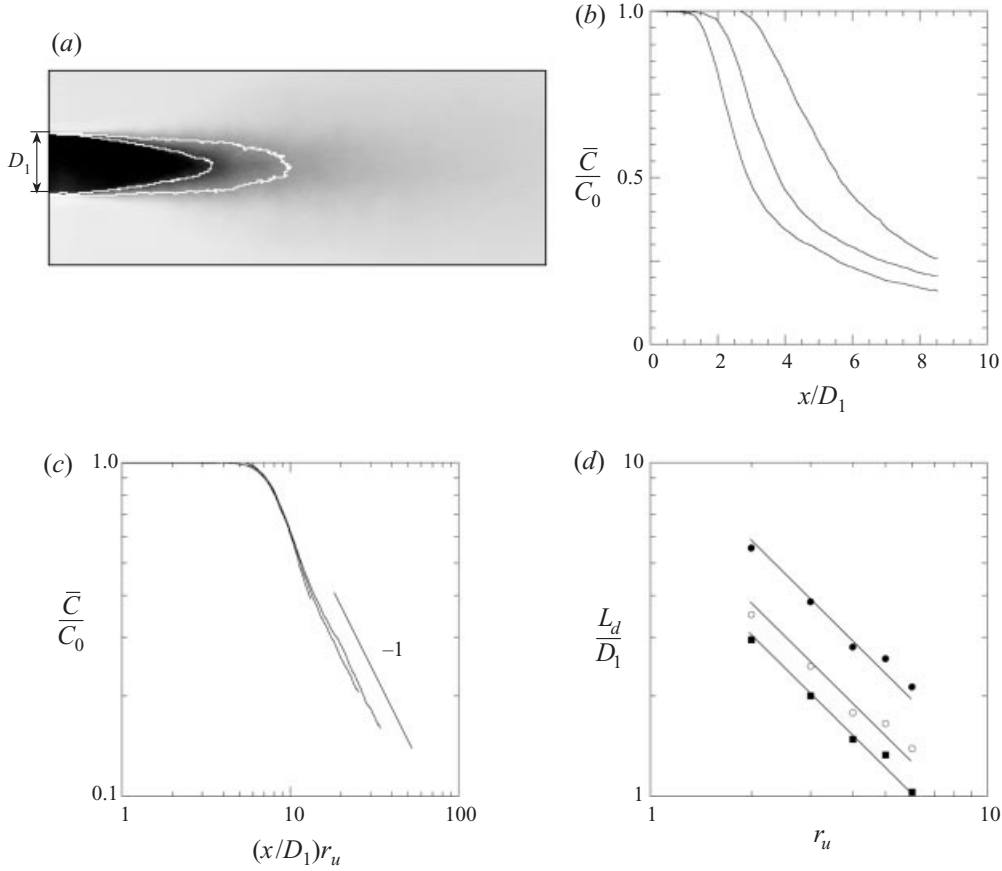
FIGURE 5. (*a*) Average concentration field of a dye injected in the central jet for $r_u = 3$. The white isoconcentration contours correspond to the dilution levels $C_s/C_0 = 0.5$ and 0.9. (*b*) Average concentration profiles along the axis, with the central jet seeded. From right to left, $r_u = 2, 3$ and 4. (*c*) Collapse of the profiles of (*b*) with the scaled spatial distance $(x/D_1)r_u$. (*d*) Dependence of the dilution lengths L_d on the velocity ratio r_u. ■, $C_s/C_0 = 0.99$; ○, $C_s/C_0 = 0.9$; ●, $C_s/C_0 = 0.5$.

3.2. *Dilution lengths*

The time needed for an instability structure of initial width $\lambda = 2\pi/k_m$ to grow up to a transverse size where it is rolled up and peeled off from the interface is of the order of $1/r$. As it will be shown in §4, the time necessary to mix it at the molecular level is longer. The entrainment velocity, which represents the size of the structures multiplied by the rate at which they are peeled off from the interface (but not necessarily mixed, see e.g. figure 6) $u_e \sim r\lambda$ is thus written as

$$u_e \sim u_2 \quad \text{for} \quad r_u = \frac{u_2}{u_1} \gg 1. \tag{4}$$

On the averaged concentration fields such as the one shown in figure 5(*a*), the isoconcentration envelopes particularized by the concentration threshold C_s have a shape intermediate between a cone and a cylinder, depending on the value of C_s/C_0. The base width is D_1 and the height of the cone is L_d. The length L_d of the isoconcentration contour can be interpreted by a scalar mass balance involving the entrainment velocity u_e. During a time interval Δt, the amount of scalar injected by
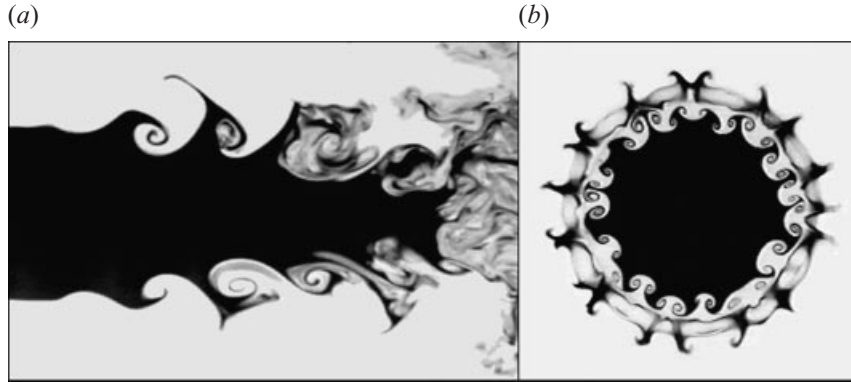
(a) (b)

FIGURE 6. Snapshots of the destabilization of the inner seeded jet by the fast annular jet for $r_u = 4$ and $Re = 1400$. (a) Planar cut containing the jet axis. (b) Transverse cut at downstream location $x = D_1/2$.

the inner jet is $\frac{1}{4}\pi D_1^2 u_1 C_0 \Delta t$. In a steady-state regime, each isoconcentration surface in the entrainment region is crossed at the velocity u_e. The quantity of scalar injected during the time Δt will thus be diluted in a volume $\pi D_1 L_d u_e \Delta t$ (for simplicity, the isoconcentration envelope is assumed to be cylindrical) down to the concentration level C_s which defines L_d. By diluted, we do not necessarily mean molecularly mixed, we just require the probability of presence of the scalar to be C_s/C_0, independently of its segregation state. The scalar mass balance is thus

$$D_1^2 u_1 C_0 \Delta t \sim L_d D_1 u_e C_s \Delta t, \tag{5}$$

providing the dependence of the dilution length L_d as a function of the velocity ratio and concentration threshold level

$$\frac{L_d}{D_1} \sim \frac{A}{r_u}\frac{C_0}{C_s}, \tag{6}$$

the constant A being found to be equal to 8 (figure 5d). The structure of the law in equation (6) is very general and is similar to the law giving the length of the potential core of the inner jet as the velocity ratio is varied, as shown by Rehab *et al.* (1997). The inner potential core length coincides with the dilution length for $C_s/C_0 = 0.9$. Equation (6) holds up to the recirculation transition (Villermaux *et al.* 1994; Rehab *et al.* 1997). The reasoning can be generalized to situations where the jets have different densities, the square root of the momentum ratio $M^{1/2} = (u_2/u_1)(\rho_2/\rho_1)^{1/2}$ replacing the velocity ratio r_u. It can also be extrapolated to the limit $M \to 0$ for the case of a single jet issuing in an environment at rest, the relevant shear velocity becoming u_1 in that case, yielding $L_d/D_1 = A(\rho_1/\rho_2)^{1/2}(C_0/C_s)$, in accordance with the compilation made by Dahm & Dimotakis (1987).

Consistent with the fact that the dilution lengths are inversely proportional to r_u for all C_s/C_0, the average concentration profiles on the jet axis of figure 5(b) collapse when the downstream coordinate is rescaled according to $(x/D_1)r_u$, as shown in figure 5(c).

At large distances x/D_1 from the end of the inner potential core, when the two jets have merged in a single jet carrying the sum of the momenta injected in each jet, the mean concentration decays as $(x/D_1)^{-1}$, as dictated by mass conservation in the far field of a round jet (figure 5c).
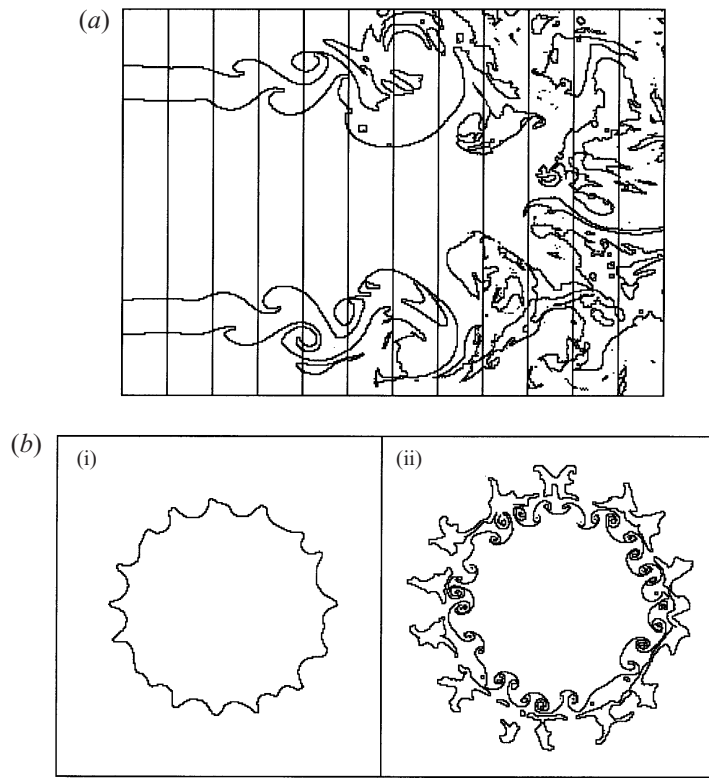
FIGURE 7. (a) Isoconcentration contour at $C_s = C_0/2$ of the image of figure 2(b), and division into successive adjacent rectangular windows of width w. (b) Transverse cuts with the inner jet seeded at (i) $x/D_1 = 1/2$ and (ii) $x/D_1 = 1$.

4. Fine structure of the mixture

Average concentrations fields and dilution lengths are indicative of the dispersion properties of one jet in the other, themselves reflecting the intensity of the entrainment rate of one jet by the other. However, dilution lengths do not provide any information about the scales involved in the entrainment process, nor about the segregation state of the mixture, that is, the contents of the flow in concentration levels intermediate between the injection concentration and zero when molecular mixing has set in.

Coaxial jets at moderate velocity ratio offer the opportunity of following step by step the sequence of events of the incorporation of one phase into the other from the initial segregation up to the onset of molecular uniformity.

4.1. *Interface generation*

The interface corrugations subsequent to the development of the instability increase the contact area between the streams. The interface area increase is significant at the end of the linear development of the instability and is directly associated with the roll-up of the crests of the instability structures, in both the spanwise and streamwise directions, as shown in figure 6.

The wavelength in the transverse direction is somewhat larger than half the wavelength in the streamwise direction, a proportion consistent with previous observations (Bernal & Roshko 1986).

The downstream evolution of the interfacial area is measured by following the
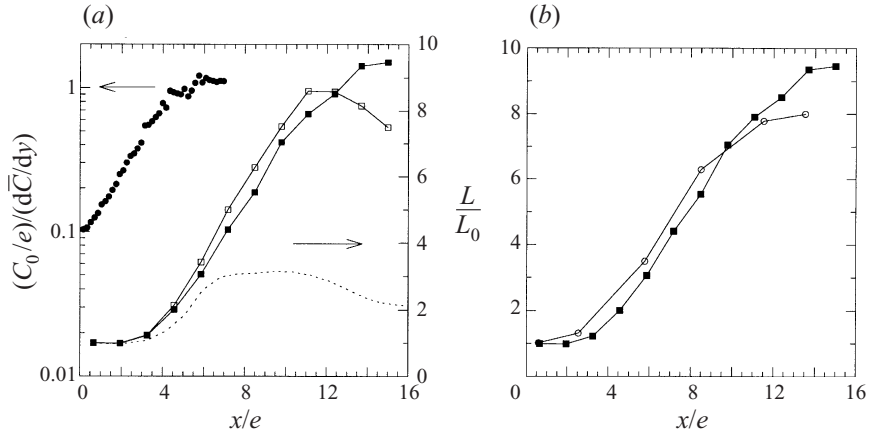
FIGURE 8. For $u_2 = 0.4\,\mathrm{m\,s^{-1}}$, $r_u = 4$, $Re = 1400$. (*a*) Simultaneous downstream evolutions of (left-hand axis) normalized concentration thickness δ_c/e and (right-hand axis) contour lengths $L_\parallel/L_0$ normalized to their initial value for ■, $C_s/C_0 = 1/2$; □, $C_s/C_0 = 2/3$. ..., evolution of the average concentration dissipation $\chi_w = \int_{S_w}\{(\mathrm{d}C/\mathrm{d}x)^2 + (\mathrm{d}C/\mathrm{d}y)^2\}\,\mathrm{d}x \times \mathrm{d}y$. (*b*) Simultaneous downstream evolutions of ■, the longitudinal $L_\parallel/L_0$ and ○, transverse $L_\perp/L_0$ contour lengths for $C_s/C_0 = 1/2$.

extent of the intercept of the isoconcentration surfaces with the visualization plane: we first extract the isoconcentration contour for a given concentration threshold C_s by a standard binarization/differentiation procedure. Then, on the longitudinal cuts, those containing the jet axes, we divide each instantaneous image into 12 adjacent rectangular windows, as shown in figure 7. The width w of each window has been chosen to be somewhat larger than the gap thickness, i.e. $w \approx 3e/2$. The length of the contour is computed in each window as the number of pixels contained in the window. The sequence of operations is repeated on 100 different images decorrelated in time, providing in each window the averaged contour length $L_\parallel$ at concentration threshold C_s. The x downstream location of the centre of the jth window is $x_j = w/2 + (j-1)w$, for $1 \leqslant j \leqslant 12$.

The same procedure of {binarization/differentiation/contour length extraction} is applied to the transverse cut images, defining the contour length $L_\perp$ at threshold C_s in the plane perpendicular to the direction of the flow for successive well-defined downstream locations. In both cases, the contributions of the spanwise and streamwise structures of the inner and outer layers are intermingled by this procedure.

In figure 8, the evolutions of the interface lengths in the longitudinal and transverse planes are displayed, together with the downstream evolution of the concentration thickness δ_c defined in equation (2). Also shown is the evolution of the component perpendicular to the plane containing the jet axes of the average concentration dissipation $\chi_w = \int_{S_w}\{(\mathrm{d}C/\mathrm{d}x)^2 + (\mathrm{d}C/\mathrm{d}y)^2\}\,\mathrm{d}x \times \mathrm{d}y$, where S_w denotes the area of the windows, normalized to its value in the first window.

It is observed that during the linear part of the instability development, that is, in the phase of exponential increase of δ_c, up to $x_c/e = 4.5$ at the Reynolds number corresponding to figure 8, the contour lengths $L_\parallel$ and $L_\perp$ representative of the interface area between the streams increase very weakly. The increase reflects the slight oscillation of the interface owing to the instability development. However, from the vicinity of the first roll-up and beyond (i.e. for $x_c/e \geqslant 4.5$ in figure 8), the contour
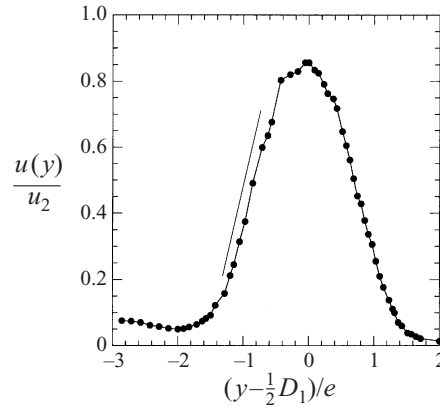
FIGURE 9. Radial profile of the mean velocity at $x/e = 6$ for $r_u = 10$.
The line has a slope equal to $1 - 1/r_u$.

lengths, in both the longitudinal and transverse directions increase markedly, as well as the dissipation χ_w.

Note that $L_\parallel$ and $L_\perp$ both grow concomitantly and at the same rate. The increase is fairly linear with downstream distance and weakly dependent on the concentration threshold C_s/C_0 chosen to define the contours up to $x/e \approx 12$. For $x/e > 12$, the evolutions of both $L_\parallel$ and $L_\perp$ saturate, then decrease and become significantly dependent on C_s/C_0. This location also corresponds to the point where the dissipation χ_w defined above starts to decrease, indicating that, after the phase of production of the interfacial area, which is the support of the scalar dissipation, the onset of molecular uniformity of the mixture follows.

These observations offer a very simple picture of the early stages of the interpenetration between the streams. Sheets of scalar whose transverse size is of the order of the primary shear instability wavelength are peeled off from the central jet and further stretched so that their linear dimensions in the streamwise and spanwise directions grow proportionally to $L_\parallel$ and $L_\perp$, respectively.

Contour lengths $L_\parallel$ and $L_\perp$ grow linearly in time, as they would if they were a material line spiralling in a vortex of constant circulation (Fung & Vassilicos 1991; Cetegen & Mohamad 1993), or a material line stretched in a parallel shear flow (see e.g. Ottino 1989). In these simple flows, the length of a material line evolves as $L(t)/L_0 = (1 + (\gamma t)^2)^{1/2}$.

The rate of elongation γ clearly coincides with the velocity gradient between the streams, involving a lengthscale which prescribes the steepness of the velocity jump $u_2 - u_1$ across the layer. There are *a priori* four different ways to estimate the velocity gradient: $(u_2 - u_1)/\delta$, $(u_2 - u_1)/e$, $(u_2 - u_1)/\lambda$ and $(u_2 - u_1)/x$. The first holds close to the injector exit, setting the instability growth rate, as already noted. The last holds far downstream from the first roll-up when the thickness of the layer grows linearly with x (Rehab *et al.* 1997). In between these extremes, the velocity gradient is of order $(u_2 - u_1)/\lambda$ when the gap width e is much larger than the primary wavelength λ (as for plane mixing layers between semi-infinite streams, Huang & Ho 1990; Karasso & Mungal 1996), and is of order $(u_2 - u_1)/e$ when $\lambda > e$. The latter condition is always fulfilled in these experiments (see equation (3) and figure 4c) and the velocity gradient is indeed found to be of order $(u_2 - u_1)/e$ after the first roll-up as shown in figure 9.

Time t and downstream distance x are linked by the mean convection velocity so

that with

$$L(t)/L_0 = (1 + (\gamma t)^2)^{1/2}, \qquad (7a)$$

and

$$\gamma = \frac{u_2}{e}(1 - 1/r_u), \quad t = 2x/u_2(1 + 1/r_u), \qquad (7b)$$

we obtain

$$\frac{L(x)}{L_0} = 2\frac{r_u - 1}{r_u + 1}\frac{x}{e} \quad \text{for } x > x_c, \qquad (7c)$$

in close agreement with the slope measured for $r_u = 4$ in figure 8 (L stands for $L_\parallel$ and $L_\perp$ indifferently).

The structure of equation (7) is identical to that giving the thickness of a shear layer separating two streams of velocity ratio r_u as a function of downstream distance x (Brown & Roshko 1974). Note that such a linear dependence holds not only for the thickness of the layer, but also for the length of material lines, or isoconcentration contours within the layer. By contrast, a succession of stretchings and foldings would have induced an exponential growth for the contour lengths, an eventuality incompatible with figure 8.

4.2. *Scale-dependent interface corrugations*

The downstream evolutions of the isoconcentration contours $L_\parallel$ and $L_\perp$ computed from two-dimensional cuts in the medium, in windows of constant surface is a direct measure of the downstream evolution of the contact surface area per unit volume between the streams. The isoconcentration surface area was found (see §4.1) to increase, before the onset of molecular mixing, like $1 + (\gamma t)^2$ since the longitudinal and transverse contour lengths were both found to evolve as $L(t) = L_0(1 + (\gamma t)^2)^{1/2}$.

The length of a contour is defined by the number of boxes $N(r)$ required to cover it multiplied by the linear size of a box r. The dependence of $N(r)$ on the scale r is informative about the process which contributes to the contour corrugation. This dependence was extracted on successive windows of instantaneous images as shown in figure 7, for a concentration threshold $C_s/C_0 = 1/2$.

We used a standard box-counting algorithm to cover the contours in each window with box sizes r smaller than the width of the window providing the $N(r)$ dependence from the resolution scale of the images up to the gap width e.

As shown on figure 10, the dependence of $N(r, x/e)$ versus r is continuously deformed as the downstream distance x/e increases. For small x/e, when the instability between the streams has not yet developed, the contour is smooth, rectilinear, and the number of covering boxes is inversely proportional to their size on the whole range of scales r/e.

From the first roll-up and farther downstream, $N(r, x/e)$ presents a more and more pronounced concave curvature. $N(r, x/e)$ is tangent to $(r/e)^{-1}$ for small r/e but the local dependence is all the more steep when the scale r compares to the gap width e and, for a given scale r, all the more steep when the downstream distance is large. The emergence of this scale-dependent fractal character is a consequence of the dependence on scale of the stirring motions themselves.

Once produced by the primary instability, the structures are progressively elongated in the sustained shear between the streams. The maximal rate of shear, giving the separation rate of two material points initially close to each other is of the order of γ given in equation 7(b). However, considering two material points belonging, for instance, to the same isoconcentration contour, initially separated by a distance r not
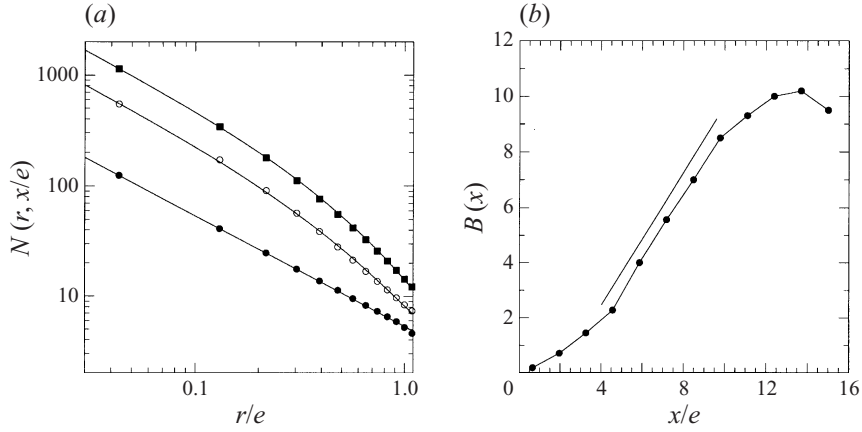
FIGURE 10. (a) Number of boxes $N(r, x/e)$ needed to cover the contours such as those of figure 7, in three successive windows at ●, $x/e = 0.65$; ○, 5.87; and ■, 12.4. The continuous lines are the fit by equation (10a) with the fitting parameter of equation (10b). $a = 1.3$. (b) Fitting parameter $B(x)$ of equation (10b) as a function of downstream distance. The line has the slope $2(r_u - 1)/(r_u + 1)$ predicted by equation (10b). $r_u = 4$, $Re = 1400$.

necessarily infinitely small, the rate at which their separation distance increases $\gamma(r)$ is smaller than γ. Velocity gradients $\delta u(r)/r$ in the flow tend to vanish, in the mean, for separation distances r larger than the scale of the mean gradient support, namely the gap width e in the present case. We thus model the elongation rate $\gamma(r) = \delta u(r)/r$ for any scale r by

$$\gamma(r) = \gamma e^{-ar/e} \quad \text{with} \quad \gamma = \frac{u_2}{e}(1 - 1/r_u), \tag{8}$$

the constant a being, by construction, of order unity. Equation (8) fulfils the required limit behaviours, that is $\gamma(r \to 0) \to \gamma$ and $\gamma(r \gg e) \to 0$. The number of boxes of size r required to cover the contour is thus, in the course of time, given by

$$N(r, t) = N(r, 0)\,[1 + (\gamma(r)t)^2]^{1/2}, \tag{9}$$

before the contour has been blurred by molecular diffusion.

Converting time to space with $t = 2x/u_2(1 + 1/r_u)$, equation (9) becomes

$$N(r, x/e) = N(r, 0)\,[1 + (B(x)e^{-ar/e})^2]^{1/2} \tag{10a}$$

with

$$B(x) = 2\frac{r_u - 1}{r_u + 1}\frac{x}{e}. \tag{10b}$$

Accounting for the initial smoothness of the contour, namely $N(r, 0) \sim r^{-1}$, the covering relationship (10) is a combination of the trivial $1/r$ factor, times a corrective factor, increasing in magnitude with time, and whose weight depends on scale: it is, at a given instant of time, a decreasing function of scale, expressing the fact that small scales have, in proportion, contributed more to the corrugation of the contour than larger scales, precisely because shearing motions are less efficient at large scales than at smaller ones (equation (8)).

The covering relationship thus exhibits a curvature, weighted by $B(x)$, and which is all the more pronounced when $B(x)$ is large (figure 10b). Choices other than an exponential can be made for the crossover function in equation (8) (see e.g. Batchelor 1951; Durbin 1980; Sawford & Hunt 1986; Villermaux & Innocenti 1999) with no
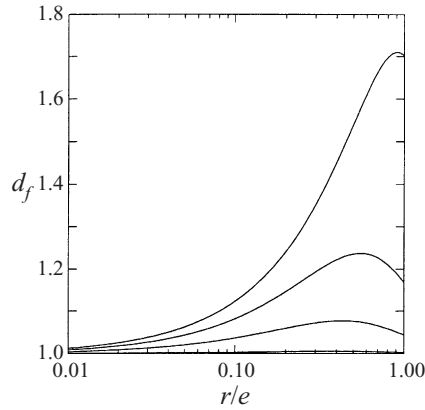
FIGURE 11. Evolution of the local fractal dimension $d_f = -\mathrm{d}\ln N(r, x/e)/\mathrm{d}\ln(r)$ through the scales r/e for successive downstream distances (from bottom to top) $x/e = 0.65, 2, 3.2$ and 5.8.

other consequence than the quality of the fit in figure 10(*a*). The absolute value of $B(x)$ and, even more, its dependence on x/e are essentially insensitive to the precise shape of the crossover function.

The weighting function $B(x)$ is actually found to coincide, in order of magnitude and in law, with the downstream development of the contour lengths $L_\parallel$ and $L_\perp$ given in equation (7) and figure 8(*a*). The rate of increase of material lengths and of their space fillingness is prescribed by the same mechanism involving the same shearing rate at the largest scale of motion γ.

A direct consequence of the scale dependence of the covering relationship (9) is the scale dependence of the fractal dimension of the contour $d_f = -\mathrm{d}\ln N(r, x/e)/\mathrm{d}\ln(r)$. This fact has been recognized in a number of related instances: the dispersion of material lines in grid turbulence (Villermaux & Gagne 1994), the conformation of isoconcentration contours in turbulent jets (Catrakis & Dimotakis 1996), of turbulent flame fronts (Pocheau & Queiros-Conde 1996) or of the shape of scalar blobs in turbulence (Villermaux & Innocenti 1999).

The local (in scale) fractal dimension has been found in these particular cases to increase from 1 at small scale, to larger values, possibly reaching 2, characteristic of space filling objects in two dimensions. The above scenario provides a mechanism for the origin of this continuous transition (see figure 11). It accounts for the observation that, at a given scale, the local dimension increases in time when a contour is followed along its transient evolution. Once molecular diffusion has become effective, this scenario also accounts for the dimension dependence on the concentration threshold level chosen to define the contour (Villermaux & Innocenti 1999).

4.3. *Onset of molecular mixing*

Unstable structures are progressively converted into sheets whose dimensions $L_\parallel$ and $L_\perp$ are increasing linearly in time. Consequently, the thickness of the sheets $s(t)$, initially of the order of the instability wavelength $s_0 \sim \lambda$, decreases, at a rate such that the volume of the structure is conserved, that is $s(t)L_\parallel L_\perp$ is conserved.

Since $L_\parallel$ and $L_\perp$ both grow approximately at the same rate, a lamella peeled off from the interface has thus a thickness given in the course of time by

$$\frac{s(t)}{s_0} = \frac{1}{1 + (\gamma t)^2} \tag{11}$$

as long as molecular diffusion of the scalar does not oppose the stretching induced thinning of the lamella.

Let C be the scalar concentration in the vicinity of the lamella and z a coordinate in the direction normal to the isoconcentration surface C. The convection–diffusion transport equation reduces (see e.g. Ranz 1979; Marble & Broadwell 1977; Marble 1988; Dimotakis & Catrakis 1999) to a one-dimensional problem when the radius of curvature of the isoconcentration surface is large compared to the lamellae thickness. In that case, the direction z aligns with the direction of maximal compression of the substrate perpendicular to the lamella and we obtain

$$\frac{\partial C}{\partial t} + \left[\frac{\partial \ln s(t)}{\partial t}\right] z \frac{\partial C}{\partial z} = D \frac{\partial^2 C}{\partial z^2}, \tag{12}$$

where $\partial \ln s(t)/\partial t$ is the rate of compression in the direction perpendicular to the lamella prescribed by its initial thinning rate. By the change of variables

$$\tau = D \int_0^t \frac{\mathrm{d}t'}{s(t')^2}, \quad \xi = \frac{z}{s(t)}, \tag{13}$$

equation (12) is reduced to a simple diffusion equation

$$\frac{\partial C}{\partial \tau} = \frac{\partial^2 C}{\partial \xi^2}. \tag{14}$$

The concentration profile across the lamella of initial width s_0 is, in the scaled coordinates of equation (13)

$$\frac{C(\xi, \tau)}{C_0} = \frac{1}{2}\left[\mathrm{erf}\left(\frac{\xi + 1/2}{2\sqrt{\tau}}\right) - \mathrm{erf}\left(\frac{\xi - 1/2}{2\sqrt{\tau}}\right)\right]. \tag{15}$$

The thickness reduction process goes on until the rate of diffusive spreading of the concentration profile across the lamella balances the rate of compression of the concentration gradient transverse to the lamella. At this critical time t_s, the maximal concentration in the lamella $C(0, t)$ falls below the initial concentration C_0 and the scalar lamella has reduced to a sheet which starts to vanish in the diluting medium. The thickness of the lamella reaches a minimum, and re-increases by diffusive spreading, as shown in figure 12. The time t_s is the mixing time relevant to that configuration. It is readily estimated by noticing that the maximal concentration $C(0, t)$ decays as soon as $\frac{1}{2}/2\sqrt{\tau}$ is of order unity and

$$t_s \sim \frac{1}{\gamma}\left(\frac{\gamma s_0^2}{D}\right)^{1/5}, \tag{16}$$

where use has been made of the expression of the warped time τ derived from equations (11) and (13), $\tau = (Dt/s_0^2)(1 + \frac{2}{3}(\gamma t)^2 + \frac{1}{5}(\gamma t)^4)$. At that time, the sheet has a thickness

$$s(t_s) \sim \frac{s_0}{(\gamma t_s)^2}, \tag{17}$$

after which, for $t \gg t_s$, the maximal concentration $C(0, t)/C_0 = \mathrm{Erf}\,[(t/t_s)^{-5/2}]$ decays as $(t/t_s)^{-5/2}$ and the sheet thickness increases diffusively as $(Dt)^{1/2}$ (figure 12).

The onset of diffusive uniformity is thus at a downstream distance equal to the critical distance for the formation of the first roll-up x_c discussed in §3.1 plus the distance travelled by the lamella during the time interval t_s. According to the values
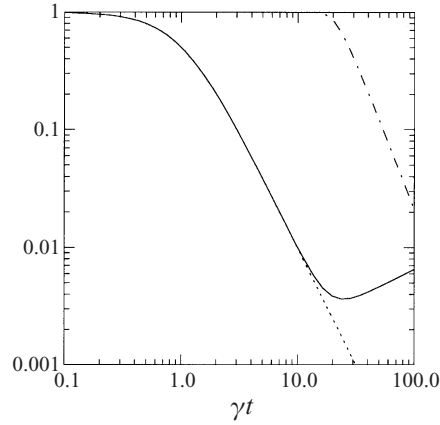
FIGURE 12. Evolutions as a function of γt and for $\gamma s_0^2/D = 2000 \times 75^2$ of: $\cdots\cdots$, thickness $s(t)/s_0$ given by equation (11); ———, thickness of the concentration profile across the lamella given by equation (15) normalized by s_0; $-\cdot-$, maximal concentration $C(0,t)/C_0$ at the centre of the sheet given by equation (15).

of x_c and $s_0 \approx \lambda$ given in equation (3), the medium is expected to have lost the trace of the initial concentration at distance

$$\frac{x_c + \bar{u}t_s}{e} = 164Re^{-1/2} + \frac{1}{2}\frac{r_u+1}{r_u-1}(50Sc)^{1/5}. \tag{18}$$

Note that the mixing time normalized by the elongation rate $\gamma t_s \approx (50Sc)^{1/5}$ is only a function of Sc, and not of the Reynolds number, precisely because of the Reynolds-number dependency of the initial size $s_0 \sim Re^{-1/2}$ (see equation (16)).

The transition distance predicted by equation (18) is approximately 13 gap widths e at $Re = 1400$, decomposed in $4.5e$ for the roll-up and lamella production period and $8.5e$ for the lamella thinning period. This overestimates the results reported on figure 8, where the transition occurs around $x/e \approx 12$. One of the possible reasons is that the dissipation scale $s(t_s)$ is not appropriately resolved on the images corresponding to figure 8.

The dissipation scale $s(t_s)$ is found, with the above estimates of γ and s_0, to be given by

$$\frac{s(t_s)}{e} = \frac{16}{Re^{1/2}Sc^{2/5}}, \tag{19}$$

and represents approximately half a pixel on the images at $Re = 1400$, thus inducing a slight underestimation of the actual transition location.

4.4. *Histograms of concentration*

The progress of mixing is quantified by following the evolution of the composition histogram, or probability density function (PDF) of the concentration fluctuations in the course of time, equivalently for successive downstream locations in an advected flow (see e.g. Koochesfahani & Dimotakis 1986). Long temporal traces of the concentration fluctuations were obtained with a fibre optic probe at the radial position $y = \frac{1}{2}D_1$ and successive downstream distances x/e, providing large samples from which PDFs can be computed down to low probability levels. The radial position was chosen to coincide with the position of the inner mixing layer.

Figure 13(a) illustrates how the scalar field, initially close to binary, as manifested
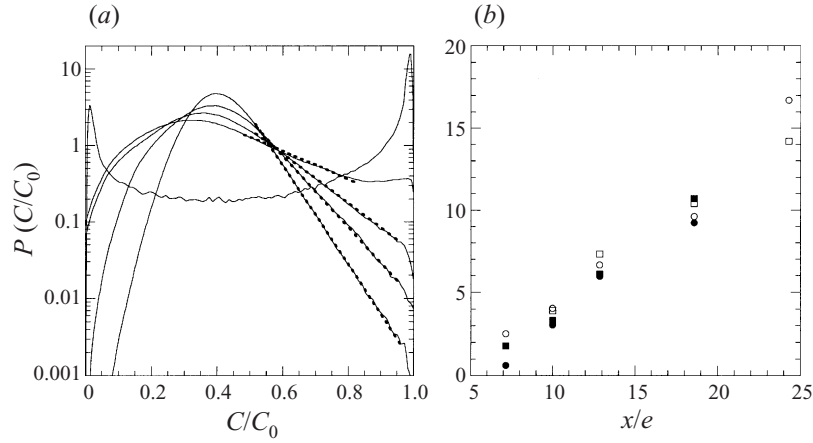
(*a*) (*b*)

FIGURE 13. (*a*) Concentration of PDFs measured at the radial position $y = \frac{1}{2}D_1$ for successive distances from the injector outlets. $x/e = 2.8$ (bimodal shape), and, with an increasing slope of the right wing exponential fall-off: $x/e = 10, 12.8, 18.5$ and 24.2. $Re = 1400$, $r_u = 4$. (*b*) Arguments of the high-concentration exponential tail for $r_u = 4$ and: $\bigcirc$, $Re = 1400$; $\blacksquare$, $Re = 2450$; $\bullet$, $Re = 3500$; $\square$, $Re = 5250$.

by its quasi-bimodal PDF with two peaks at the injection concentration and at the diluting concentration, progressively evolves towards a unimodal shape, with a maximum around the mean composition of the mixture. The composition of the medium still bears the memory of the initial segregation at $x/e = 10$, but, farther downstream, the injection concentration in the inner jet has virtually disappeared in the medium since it is rejected to very low, and ever-decreasing probability levels.

Of interest is the right wing of the PDFs, representative of the highest concentration levels in the medium. These are carried by the lamellae peeled-off from the entrained inner jet and diluting in the outer one in which they have been sufficiently stretched to reach the dissipative scale and in which they have therefore started to diffuse. The right wing of the PDF, that we denote $P_>(C/C_0)$, is thus a measure of the relative number of sheets bearing a maximal concentration C. It is observed, as shown on figure 13(*a*), to decrease fairly exponentially, with an argument increasing roughly linearly with downstream location x/e above a critical distance x_s/e as

$$P_> \left(\frac{C}{C_0} \right) \sim \exp \left(-\frac{x - x_s}{e} \frac{C}{C_0} \right) \quad \text{with} \quad x_s/e \approx 7. \qquad (20)$$

The critical distance x_s, below which the PDFs are still reflecting the initial segregation and no clear, regular fall-off can be detected on the high concentration wing is smaller than $x_c + \bar{u} t_s$ given in equation (20). The distance x_s corresponds to the beginning of the plateau of the dissipation χ_w discussed in §4.1 and figure 8, whereas $x_c + \bar{u} t_s$ is the location of the end of the plateau, where the initial concentration is no longer present in the mixture.

The exponential form (19) is very general and is encountered in several different situations of both active (Castaing *et al.* 1989) and passive scalar mixing (Jayesh & Warhaft 1992; Thoroddsen & Van Atta 1992; Villermaux, Innocenti & Duplat 1998). It has prompted some interpretations (Pumir, Shraiman & Siggia 1991, Shraiman & Siggia 1994). We have suggested (Villermaux *et al.* 1998) that this shape is a consequence of the distribution of the cumulated stretchings experienced by the different fluid particles in the flow at a given instant of time. The elongation of a

lamella is given, at time t, by the product γt, in the mean. However, some lamellae have been more elongated, and others less than the mean. The elongation, and therefore the time a onset of diffusive mixing thus fluctuates from one lamella to the other as a result of the ubiquitous randomness of turbulent flows.

It is, from there, straightforward to show that a distribution of the individual elongations n around the mean $\bar{n} = \gamma t$ results for the highest concentrations wing of the PDF in an exponential fall-off. Let $\mathscr{P}(n)$ be the distribution of the elongations n a time t. Its structure has to reflect the fact that the existence of different histories among a population of lamellae at a given finite time results from the finiteness of $\bar{n}$. The distribution of cumulated stretchings and therefore of n becomes narrower relative to the mean as time elapses, expressing the fact that the scalar lamellae in the population tend to have similar histories as time progresses. This is accounted for by, for instance, imposing the proportionality of the variance of the distribution $\mathscr{P}(n)$ to its mean $\bar{n}$. Among others, the Poisson distribution $\mathscr{P}(n) = n^{\bar{n}-1} \exp{(-\bar{n})}/n!$ presents this property.

With $C(0,t)/C_0 = \text{Erf}\,[(t/t_s)^{-5/2}]$, the high concentration side of the concentration PDF is well approximated by

$$P_> \left(\frac{C}{C_0} \right) \sim \exp \left(-(\bar{n} - n_s)\frac{C}{C_0} \right), \tag{21}$$

where n_s is the elongation at the mixing time γt_s. The influence of the precise shape of the distribution $\mathscr{P}(n)$ on the final concentration distribution is very weak. Of crucial importance for the value of its argument is, however, the width of the distribution, measured by $\bar{n}^{1/2}$ at the mixing-time elongation n_s.

Using the transformations of equation (7*b*) we thus expect the argument of the right wing of the concentration PDF to increase at the same rate with downstream distance as the length of isoconcentration contours before the onset of molecular mixing (7) and of the curvature parameter $B(x)$ of the covering relationship (10), namely $2(r_u - 1)/(r_u + 1)x/e$, independently of the Reynolds number. This is in good agreement, at least in order of magnitude, with the measured slopes reported on figure 13(*b*). They are also expected to be independent of the Schmidt number.

Beyond the relatively fair quantitative agreement of this simple model for the PDF, its interest relies on its consistency with the observed fact that the lamella transverse scale reduction process is mediated by a coherent, persistent shear, as discussed in §4.1 and shown in figure 8. The rate of uniformity of the mixture at the molecular level follows the rate of increase of material lines, itself prescribed by a shear γ sustained at a scale much larger than the dissipation scale $s(t_s)$.

5. Spectra

The power spectrum of the concentration fluctuations reflects, close to the injector outlets, the passage of the periodic disturbances produced by the primary instability. When the measurement location is chosen to be close to the first roll-up (see figure 14), the spectrum presents a broad peak centred at the frequency f equal to the passage frequency, i.e. $f\lambda/\bar{u} = 1$, where λ denotes the instability wavelength given in equation (3).

Farther downstream, after the onset of molecular mixing, the spectrum loses progressively the memory of the instability periodicity to give way to a power-law-like shape (figure 15*a*), whose exponent is close to -1. This power-law-like decrease
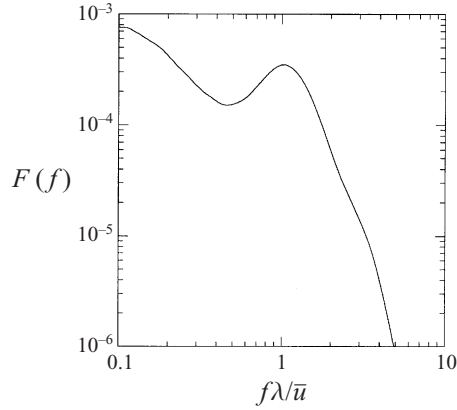
FIGURE 14. Concentration fluctuation spectrum measured at the radial position $y = \frac{1}{2}D_1$ and downstream distances $x/e = 2.8$. $Re = 1400$.
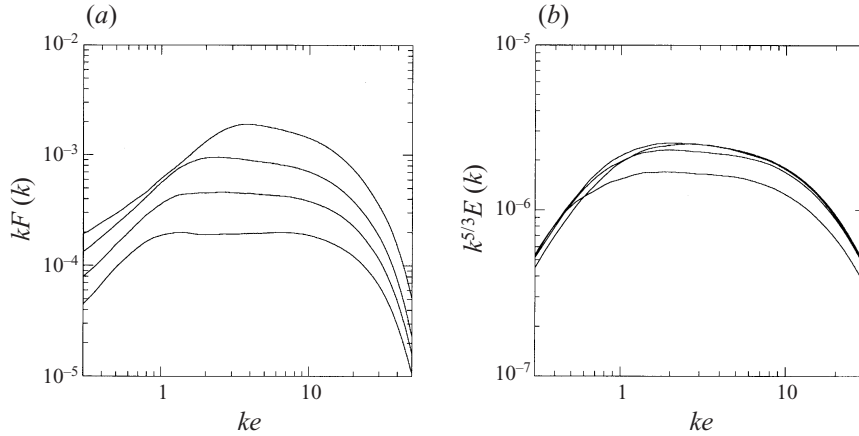

FIGURE 15. (*a*) Concentration fluctuation spectra measured at the radial position $y = \frac{1}{2}D_1$ for successive distances from the injector outlets. $x/e = 10, 12.8, 18.5$ and 24.2. The corresponding concentration PDFs are shown in figure 14. (*b*) Velocity fluctuation spectra measured at the same positions. $Re = 1400$, $r_u = 4$.

extends from the gap width (i.e. $ke = 1$ with the wavenumber k defined by $k\bar{u} = 2\pi f$) to smaller scales down to the resolution scale of the probe (i.e. $ke \approx 20$).

At the same locations in the flow, the power spectrum of the velocity fluctuations displays a clearly steeper, power-law-like decrease on the same range of scales (figure 15*b*). The apparent exponent, if any, is close to $-5/3$, consistent with known results in mixing layers after the mixing transition (Huang & Ho 1990).

A number of investigations have observed that the spectrum of a passive scalar mixed in a turbulent flow usually exhibits a dependence less steep than $k^{-5/3}$ in the inertial range of scales (Miller & Dimotakis 1996; Sreenivasan 1996; Mydlarski & Warhaft 1998 and references therein), the phenomenon being particularly marked in shear flows. This fact can interestingly be put in relation to the permanence of the large-scale straining motions in the scalar transverse scale reduction process during the route towards dissipation we have described before (§4).

Concerning the interface area generation between the streams (§4.1), the emergence

of a scale-dependent roughness of the isoconcentration contours (§4.2) as well as the rate at which the initial segregation evolves towards uniformity after the mixing transition (§4.3), we have found that the clock which sets the kinetics of these various manifestations of the mixing between the streams, before, and after the onset of molecular mixing, is the large-scale turnover time γ^{-1}. We underline now the spectral consequences of the persistence of this large-scale motion.

If $F(k)$ denotes the power spectrum of the concentration signal, the fraction of the variance C'^2 carried by a wavenumber bandwidth Δk around the wavenumber k is $F(k)\Delta k$. During a time interval Δt in the course of the thinning of a scalar lamella given by equation (11), the wavenumber $k(t)$ increases to $k(t + \Delta t) = k'$ such that

$$\frac{k'}{k} = \frac{1 + (\gamma(t + \Delta t))^2}{1 + (\gamma t)^2}. \tag{22}$$

The bandwidth $\Delta k(t)$ increases to $\Delta k(t + \Delta t) = \Delta k'$ accordingly. Thus, for $t < t_s$, that is as long as the wavenumber k has not reached the dissipation wavenumber $k_s = 1/s(t_s)$, the energy $F(k)\Delta k$ contained in the bandwidth $\Delta k(t)$ is constant and the spectrum is such that

$$kF(k) = \text{constant} \quad \text{for} \quad k < 1/s(t_s). \tag{23}$$

The above argument is, in essence, the one invoked by Batchelor (1959) in discussing the shape of the scalar power spectrum for scales below the Kolmogorov scale in a turbulent flow. The k^{-1} shape originates in this view from the fact that the intensity of the straining motions which distort the scalar field around a wavenumber k do not depend on k.

The permanence of the elongation rate γ in the course of the scalar scale reduction process is such that it induces persistent enough stretchings to 'bypass' the pre-existing hierarchy of scales in the flow, whose structure is reflected by the close-to-$k^{-5/3}$ spectrum of the velocity field. This 'cascade bypass' in the inertial range of scales has to be contrasted with the traditional description of scalars being advected in a turbulent flow (Oboukhov 1949; Corrsin 1951).

6. Discussion and conclusions

The objective of this study was to discover the minimal set of ingredients required to understand the progress of mixing in a prototype shear flow, namely coaxial jets with outer to inner velocity ratio larger than unity.

We were first interested in describing global quantities, as dilution lengths of the inner jet in the outer destabilizing jet. We have shown that the entrainment velocity can be understood from the primary shear instability between the phases. Since the selected wavelength λ and its growth rate r are, respectively, in direct and inverse proportion of the vorticity thickness δ of the fast stream velocity profile at the injector lip, their product, giving the entrainment velocity, is found simply to be proportional to the velocity difference absorbed by the inner layer. Thus, the dilution length L_d, measured at a given threshold concentration C_s, is solely determined by the velocity ratio $r_u = u_2/u_1$ and the relative concentration threshold C_s/C_0. We also depicted the chronology of events of the interpenetration between the streams, up to the onset of the diffusive uniformity. The present work suggests that the only two quantities necessary to understand the rate of interface corrugation, the time of onset of molecular mixing and the subsequent rate of change of the medium composition are the initial vorticity thickness δ, set by the initial Reynolds number

Re, and the elongation rate $\gamma = (u_2/e)(1 - 1/r_u)$ constructed with the net velocity difference between the streams and the gap width e.

For a given gap width, the Reynolds number fixes the downstream distance of the first roll-up, and the instability wavelength. Both are proportional to δ, which also fixes the order of magnitude of the initial transverse thickness of the lamella peeled-off from the slow jet. The shorter the instability wavelength, that is, the thinner the initial structures, the earlier they reach the dissipative scale. The transverse thickness reduction process is mediated by the large-scale rolling-up structures in the shear layer, in both the streamwise and spanwise directions. Their role is evidenced by the omnipresence of the Brown–Roshko factor $(r_u - 1)/(r_u + 1)$ in the spatial growth of the isoconcentration contour lengths $L_\parallel$ and $L_\perp$, the curvature parameter of the covering law $N(r, x/e)$, and the evolution of the highest concentration wing of the composition PDFs after the mixing transition. All of these quantities evolve as γt which, when time has been transformed to space equals $2(r_u - 1)/(r_u + 1)x/e$. These observations are consistent with earlier observations in plane mixing layers. Bradshaw (1966), Breidenthal (1981) and Roshko (1991) insisted on the role played by the initial conditions (i.e. the thickness of the velocity profiles at the splitter plate lip) on the earliness of the mixing transition. Huang & Ho (1990) and Karasso & Mungal (1996) have shown how the location of the transition downstream of the splitter lip is best collapsed among different operating conditions when the downstream distance x is rescaled by the initial wavelength and the Brown–Roshko factor as $(r_u - 1)/(r_u + 1)x/\lambda$ (as explained in §4.1, λ replaces the gap width e when $\lambda < e$, as for plane mixing layers between semi-infinite streams).

Koochesfahani & Dimotakis (1986) and Dimotakis & Catrakis (1999) have nevertheless pointed out that the local Reynolds number of the layer has to be large enough to allow the destabilization of internal shear layers for the transition to happen, via the formation of small scales compared to the width of the layer. The separation of scales is indeed a crucial ingredient which distinguishes laminar (i.e. with a single scale) from turbulent mixing. The initial size $s_0 \sim eRe^{-1/2}$ of the structures which will be further stretched and mixed is smaller, decreasing with Re, than the scale over which extends the support of the elongation γ, namely e. This is the condition for the mixing time $t_s \sim (1/\gamma)(\gamma s_0^2/D)^{1/5}$ to be Reynolds number invariant, as suggested by the experiments. The destabilization of the initial shear layer leading to the formation of the structures of size $s_0 \sim \lambda \sim \delta$ must, therefore, be possible. For this, the Reynolds number Re_δ based on the initial profile thickness δ must be large enough, otherwise the shear instability is smoothed out by viscous spreading (see also the discussion in Villermaux 1998*b*).

The above form of t_s, involving an elongation of material lines linear in time because of the persistence of a mean shear, is peculiar to the situation studied here. An exponential growth of material lines and surfaces would be characterized, following the procedure described in §4.3, by a mixing time given by $t_s \sim (1/\gamma)\ln(\gamma s_0^2/D)$ but the conclusions would remain the same.

The persistence of the large-scale straining motions and the omnipresence of the factor γt before and after the onset of molecular mixing has led us to define a scalar dissipation scale $s(t_s)$ which results from a stretching assisted diffusion problem with a single scale elongation rate γ. The scale for which molecular diffusion opposes the stretching induced substrate compression is only a function, again, of the initial profile thickness δ via s_0, and of the Schmidt number Sc. The dissipation scale inferred from this balance $s(t_s) \sim eRe^{-1/2}Sc^{-2/5}$ is, *de facto*, different from the Batchelor scale, itself linked to the Kolmogorov scale. Although the spectra reported here were not capable

of assessing the existence of this dissipation scale, because they are not resolved enough in scale, there is some evidence to suggest it: nowhere in the course of this study, in which mixing has been contemplated according to its different facets, have we found the manifestation of a sequential cascade process, nor even of a multiplicative process, e.g. contour lengths grow linearly in time, the composition of the medium at a given location is fairly insensitive to the Reynolds number, concentration spectra decay as k^{-1}. Our findings offer a different perspective for scalars advected in a turbulent flow. Large-scale motions produce internal shear layers which destabilize to form structures whose size decrease with the Reynolds number as $Re^{-1/2}$. These structures are further stretched at the rate prescribed by the large-scale motions before they are dissipated. A direct connection is thus permanently established between injection scales and dissipative scales, the broad distribution of the quantities which characterize the mixture (composition, spectrum) being the reflection of distributed histories among the population of structures.

REFERENCES

BATCHELOR, G. K. 1951 Pressure fluctuations in isotropic turbulence. *Proc. Cam. Phil. Soc.* **47**, 359–374.

BATCHELOR, G. K. 1959 Small-scale variation of convected quantities like temperature in a turbulent fluid. Part 1. General discussion and the case of small conductivity. *J. Fluid Mech.* **5**, 113–133.

BECKER, H. A. & MASSARO, T. A. 1968 Vortex evolution in a round jet. *J. Fluid Mech.* **31**, 435–448.

BEÉR, J. M. & LEE, K. B. 1965 The effect of the residence time distribution on the performance and efficiency of combustors. *Third Symp. (Intl) on Combustion*, pp. 1187–1202. The Combustion Institute.

BERNAL, L. P. & ROSHKO, A. 1986 Streamwise vortex structure in plane mixing layers. *J. Fluid Mech.* **170**, 449–525.

BETCHOV, R. & SZEWCZYK, G. 1963 Stability of a shear layer between parallel streams. *Phys. Fluids* **6**, 1391–1396.

BRADSHAW, P. 1966 The effect of initial conditions on the development of a free shear layer. *J. Fluid Mech.* **26**, 225–236.

BREIDENTHAL, R. 1981 Structure in turbulent mixing layers and wakes using a chemical reaction. *J. Fluid Mech.* **109**, 1–24.

BROWN, G. L. & ROSHKO, A. 1974 On density effects and large structure in turbulent mixing layers. *J. Fluid Mech.* **64**, 775–816.

CASTAING, B., GUNARATNE, G., HESLOT, F., KADANOFF, L., LIBCHABER, A., THOMAE, S., WU, X. Z., ZALESKI, S. & ZANETTI, G. 1989 Scaling of hard thermal turbulence in Rayleigh–Bénard convection *J. Fluid Mech.* **204**, 1–30.

CATRAKIS, H. J. & DIMOTAKIS, P. E. 1996 Mixing in turbulent jets: scalar measures and isosurface geometry. *J. Fluid Mech.* **317**, 369–406.

CETEGEN, B. M. & MOHAMAD, N. 1993 Experiments on liquid mixing and reaction in a vortex. *J. Fluid Mech.* **249**, 391–414.

CORRSIN, S. 1951 On the spectrum of temperature fluctuations in an isotropic turbulence. *J. Appl. Phys.* **22**, 469–473.

DAHM, W. J. A., CLIFFORD, E. F. & TRYGGVANSON, G. 1992 Vortex structure and dynamics in the near field of a coaxial jet. *J. Fluid Mech.* **241**, 371–402.

DAHM, W. J. A. & DIMOTAKIS, P. E. 1987 Measurements of entrainment and mixing in turbulent jets. *AIAA J.* **25**, 1216–1223.

DIMOTAKIS, P. E. 1991 Turbulent free shear layer mixing and combustion. *Progress in Astronautics and Aeronautics*, vol. 137. AIAA.

DIMOTAKIS, P. E. & CATRAKIS, H. J. 1999 Turbulence, fractals and mixing. In *Mixing: Chaos and Turbulence* (ed. H. Chaté, E. Villermaux & J. M. Chomaz). Kluwer/Plenum.

DURBIN, P. A. 1980 A stochastic model for two particle dispersion and concentration fluctuations in homogeneous turbulence. *J. Fluid Mech.* **100**, 279–302.

ESCH, R. E. 1957 The instability of a shear layer between two parallel streams. *J. Fluid Mech.* **3**, 279–302.

FREYMUTH, P. 1966 On transition in a separated laminar boundary layer. *J. Fluid Mech.* **25**, 683–704.

FUNG, J. C. H. & VASSILICOS, J. C. 1991 Fractal dimension of lines in chaotic advection. *Phys. Fluids* A **3**, 2725–2733.

HUANG, L.-S. & HO, C.-M. 1990 Small-scale transition in a plane mixing layer. *J. Fluid Mech.* **210**, 475–500.

JAYESH & WARHAFT, Z. 1992 Probability distributions, conditional dissipation, and transport of passive temperature fluctuations in grid-generated turbulence. *Phys. Fluids* A **4**, 2292–2307.

KARASSO, P. S. & MUNGAL, M. G. 1996 Scalar mixing and reaction in plane liquid shear layers. *J. Fluid Mech.* **323**, 23–63.

KOOCHESFAHANI, M. M. & DIMOTAKIS, P. E. 1986 Mixing and chemical reaction in a turbulent liquid mixing layers. *J. Fluid Mech.* **170**, 83–112.

LEFEBVRE, A. H. 1989 *Atomization and Sprays*. Hemisphere, Taylor and Francis.

MARBLE, F. E. 1988 Mixing, diffusion and chemical reaction of liquids in a vortex field. *Chemical Reactivity in Liquids: Fundamental Aspects* (ed. M. Moreau & P. Turq). Plenum.

MARBLE, F. E. & BROADWELL, J. E. 1977 The coherent flame model for turbulent chemical reactions. *Project SQUID, Tech. Rep. TRW-9-PU.*

MILLER, P. L. & DIMOTAKIS, P. E. 1996 Measurements of scalar power spectra in high Schmidt number turbulent jets. *J. Fluid Mech.* **308**, 129–146.

MONKEWITZ, P. & HUERRE, P. 1982 Influence of the velocity ratio on the spatial instability of mixing layers. *Phys. Fluids* **25**, 1137–1143.

MYDLARSKI, L. & WARHAFT, Z. 1998 Passive scalar statistics in high-Péclet-number grid turbulence. *J. Fluid Mech.* **358**, 135–175.

OBOUKHOV, A. M. 1949 Structure of the temperature field in a turbulent flow. *Izv. Acad. Nauk SSSR, Geogr. i Geofiz.* **13**, 58–69.

OTTINO, J. M. 1989 *The Kinematics of Mixing: Stretching, Chaos, and Transport*. Cambridge University Press.

POCHEAU, A. & QUEIROS-CONDE, D. 1996 Transition from Euclidean to fractal forms within a scale-covariant process: a turbulent combustion study. *Europhys. Lett.* **35**, 439–444.

PUMIR, A., SHRAIMAN, B. I. & SIGGIA, E. D. 1991 Exponential tails and random advection. *Phys. Rev. Lett.* **66**, 2984–2987.

RANZ, W. E. 1979 Application of a stretch model to mixing, diffusion and reaction in laminar and turbulent flows. *AIChE J.* **25**, 41–47.

RAYLEIGH, LORD 1880 On the stability, or instability of certain fluid motions. *Proc. Lond. Math. Soc.* **11**, 57–70.

REHAB, H., VILLERMAUX, E. & HOPFINGER, E. J. 1997 Flow regimes of large velocity ratio coaxial jets. *J. Fluid Mech.* **345**, 357–381.

ROSHKO, A. 1991 The mixing transition in free shear flows. In *The Global Geometry of Turbulence*, (ed. J. Jiménez). Kluwer/Plenum.

SAWFORD, B. L. & HUNT, J. C. R. 1986 Effects of turbulence structure, molecular diffusion and source size on scalar fluctuations in homogeneous turbulence. *J. Fluid Mech.* **165**, 373–400.

SHRAIMAN, B. I. & SIGGIA, E. D. 1994 Lagrangian path integrals and fluctuations in random flows. *Phys. Rev.* E **49**, 2912–2927.

SLESSOR, M. D., BOND, C. L. & DIMOTAKIS, P. E. 1998 Turbulent shear-layer mixing at high Reynolds numbers: effects of inflow conditions. *J. Fluid Mech.* **376**, 115–138.

SQUIRE, H. B. 1953 Investigation of the stability of a moving liquid film. *British J. Appl. Phys.* **4**, 167–169.

SREENIVASAN, K. R. 1991 Fractals and multifractals in fluid turbulence. *Ann. Rev Fluid Mech.* **23**, 539–600.

SREENIVASAN, K. R. 1996 The passive scalar spectrum and the Obukhov–Corrsin constant. *Phys. Fluids* **8**, 189–196.

THORODDSEN, S. T. & VAN ATTA, C. W. 1992 Exponential tails and skewness of density-gradient probability density functions in stably stratified turbulence. *J. Fluid Mech.* **244**, 547–566.

VAN ATTA, C. W. & CHEN, W. Y. 1970 Structure functions of turbulence in the atmospheric boundary layer over the ocean. *J. Fluid Mech.* **44**, 145–159.

VILLERMAUX, E. 1998*a* Mixing and spray formation in coaxial jets. *J. Prop. Power* **14**, 807–817.

VILLERMAUX, E. 1998*b* On the role of viscosity in shear instabilities. *Phys. Fluids* **10**, 368–373.

VILLERMAUX, E. & GAGNE, Y. 1994 Line dispersion in homogeneous turbulence: stretching, fractal dimensions and micromixing. *Phys. Rev. Lett.* **73**, 252–255.

VILLERMAUX, E. & INNOCENTI, C. 1999 On the geometry of turbulent mixing. *J. Fluid Mech.* **393**, 123–145.

VILLERMAUX, E., INNOCENTI, C. & DUPLAT, J. 1998 Scalar fluctuations PDF's in transient turbulent mixing. *C. R. Acad. Sci. Paris*, IIb, **326**, 21–26.

VILLERMAUX, E., REHAB, H. & HOPFINGER, E. J. 1994 Breakup regimes and self-sustained pulsations in coaxial jets. *Meccanica* **29**, 393–401.

WELANDER, P. 1955 Studies on the general development of motion in a two-dimensional, ideal fluid. *Tellus* **7**, 141–156.

WILLIAMS, F. A. 1985 *Combustion Theory*. Addison–Wesley.